

Caustic effects on the high-order harmonic generation in graphene

Fulong Dong, Jie Liu*

Graduate School, China Academy of Engineering Physics, Beijing 100193, China

(Dated: March 14, 2023)

We have investigated the caustic effects on the high-order harmonic generation (HOHG) in graphene. By numerically simulating the HOHG by the two-band density-matrix equations and time-dependent density functional theory, we find obvious caustic structures on the HOHG. Further calculations indicate that the caustic effects exist over a wide range of laser vector potential from 0.4 to 0.84 a.u.. To reveal the underlying mechanism of the caustic effects, we calculate the classical trajectories of electrons. For a one-dimensional section of the graphene reciprocal space, when the different branches of electron-hole trajectories generating high-order harmonics coalesce into a single branch, caustic effects appear. In contrast to atom and one-dimensional solid, in which the caustic effects usually appear at a or a few specific harmonic energies, for the two-dimensional graphene system, the caustic effects emerge in broad, continuous energy regions, which dominates interband harmonic generation.

I. INTRODUCTION

As light propagates, focusing usually occurs. Multiple rays of light can coalesce and form bright focusing features known as caustics [1]. These features are singularities of optics, and their intensity may diverge to some extent. The enhancement of the intensity is predicted by catastrophe theory, where each caustic can be associated with a catastrophe class that dictates its properties [2, 3].

With the rapid development of laser technology, high-order harmonic generation from the gases of atoms and molecules has been widely studied over the past several decades [4–7]. In recent years, much attention also has been given to harmonic generation in crystalline solids [8–12] and some two-dimensional materials [13, 14].

Naturally, caustic effects in the high-order harmonic generation (HOHG) has attracted interest. For gases, the singularity, where the long and short trajectories of recollision electrons coalesce into a single trajectory, has been known to cause caustic enhancement in the spectrum [15–17]. Recently, caustic effects of HOHG also been observed in the one-dimensional periodic potential model, as the different branches of electron hole trajectories generating high-order harmonics coalesce into a single branch [18]. Besides, the van Hove singularities of the energy band structure in solids also have been reported to result in the spectral caustics in high-order harmonic generation [19].

Graphene is a simple but specific two-dimensional material, in which there are only two carbon atoms per unit cell and the atoms are orderly arranged in a periodic hexagonal lattice. The unique electronic structure of graphene [20, 21] exhibits a variety of nonlinear optical processes [22–26]. In this work, we study the caustic effects on the HOHG in graphene. We numerically calculate the HOHG by the two-band density-matrix equations and time-dependent density functional theory, respectively, and the results both show obvious caustic structures. Further calculations show that the caustic effects exist over a wide range of laser vector potential from 0.4 to 0.84 a.u.. Based on the classi-

cal trajectory of electrons in the real space, we reveal the underlying mechanism of the caustic effects. For a one-dimensional section of the graphene reciprocal space, when the different branches of electron-hole trajectories generating high-order harmonics coalesce into a single branch, caustic effects appear. In contrast to atom and one-dimensional solid, in which the caustic effects usually appear at a or a few specific harmonic energies, for the two-dimensional graphene system, the caustic effects emerge in broad, continuous energy regions, which dominates interband harmonic generation.

This paper is organized as follows. We describe our physical model in Sec. II. Section III shows caustic effects on the high-order harmonic generation in graphene. Finally, Sec. IV presents our conclusion. Throughout the paper, atomic units are used if not specified.

II. PHYSICAL MODEL

A. Graphene structure

Graphene is a two-dimensional single layer of carbon atoms arranged in a honeycomb lattice structure [21] as shown in Fig. 1(a), which consists of two sublattices with atoms labeled “A” and “B”. The lattice vectors ($\mathbf{a}_1 = (3, \sqrt{3})d/2$ and $\mathbf{a}_2 = (3, -\sqrt{3})d/2$ where $d = 1.42$ Å is the carbon-carbon distance) and the nearest-neighbor vectors ($\mathbf{\delta}_i$, $i = 1, 2, 3$) are also presented in Fig. 1(a). The first Brillouin zone of graphene is shown in Fig. 1(b), in which $\mathbf{b}_1 = 2\pi(1, \sqrt{3})/3d$ and $\mathbf{b}_2 = 2\pi(1, -\sqrt{3})/3d$ are the reciprocal-lattice vectors and high symmetry points (Γ , M and K) are marked. In Figs. 1(a) and 1(b), \mathbf{e} is the unit vector that indicates the polarization direction of the infrared (IR) laser field.

Utilizing the Bloch states as the basis set, the tight-binding Hamiltonian H_0 arising from the π orbitals of graphene has the form $H_0 = \begin{pmatrix} 0 & \gamma_0 f(\mathbf{k}) \\ \gamma_0 f^*(\mathbf{k}) & 0 \end{pmatrix}$, in which electrons can only hop to nearest-neighbor atoms with hopping energy of $\gamma_0 = 0.1$ a.u., and

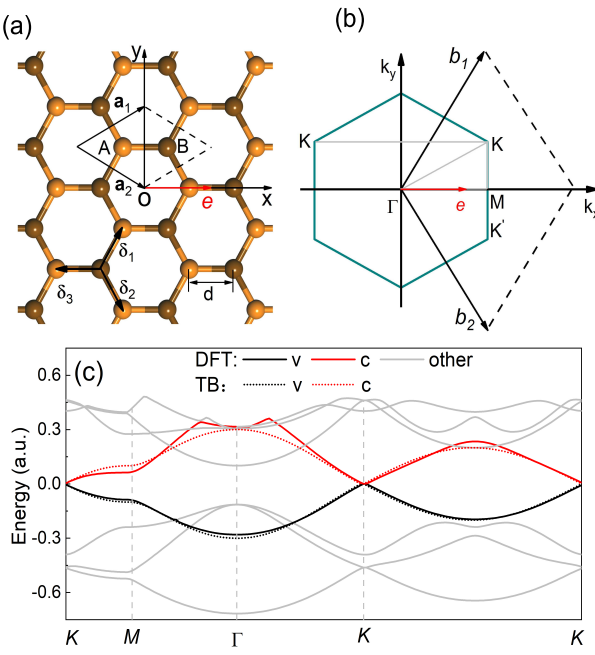


Figure 1. (a) Hexagonal lattice structure of two-dimensional graphene. Each primitive cell contains two atoms labeled “A” and “B”. \mathbf{a}_1 and \mathbf{a}_2 are the lattice vectors and δ_i , $i = 1, 2, 3$, are the nearest-neighbor vectors. \mathbf{e} is the unit vector that indicates the polarization direction of the electric field. d is the carbon-carbon distance. (b) First Brillouin zone of graphene with high symmetry points Γ , M and K . \mathbf{b}_1 and \mathbf{b}_2 are the reciprocal-lattice vectors. (c) The dispersion relations of energy bands calculated by the tight-binding (TB) approximation and the density functional theory (DFT) along the direction of K - M - Γ - K - K as shown by the grey lines in (b).

$f(\mathbf{k}) = e^{i\mathbf{k}_x d} + 2 \cos(\sqrt{3}\mathbf{k}_y d/2) e^{-i\mathbf{k}_x d/2}$. Diagonalization of the H_0 matrix can yield energy eigenvalues, which describe the dispersion relations of the conduction (c) and valence (v) bands $\varepsilon_c(\mathbf{k}) = -\varepsilon_v(\mathbf{k}) = \gamma_0 |f(\mathbf{k})| = \gamma_0 \sqrt{3 + 2 \cos(\sqrt{3}\mathbf{k}_y d) + 4 \cos(3\mathbf{k}_x d/2) \cos(\sqrt{3}\mathbf{k}_y d/2)}$, which have been shown by the red and black dotted lines in Fig. 1(c), respectively. For comparison, we have also shown the energy bands of graphene which are calculated by the density functional theory (DFT) in Fig. 1(c). One can find that the conduction and valence bands of the tight-binding model is approximately consistent with those of DFT.

B. Two-band density-matrix equations

We numerically simulate the HOHG of graphene by the two-band density-matrix equations (TBDMEs) in Houston basis [27]. Within the dipole approximation, these

equations read

$$i \frac{d}{dt} \rho_{mn}(\mathbf{K}(t), t) = [\varepsilon_{mn}(\mathbf{K}(t)) - i\Gamma_{mn} \frac{\tilde{\delta}_{mn}}{T_2}] \rho_{mn}(\mathbf{K}(t), t) + \mathbf{E}(t) \cdot \sum_l [\mathbf{D}_{ml}(\mathbf{K}(t)) \rho_{ln}(\mathbf{K}(t), t) - \rho_{ml}(\mathbf{K}(t), t) \mathbf{D}_{ln}(\mathbf{K}(t))], \quad (1)$$

where $\hat{\rho}$ is the density matrix comprising elements $\rho_{mn} = \langle m, \mathbf{k} | \rho | n, \mathbf{k} \rangle$, where m and n represent the valence or conduction band. In Eqs. (1), we consider $\varepsilon_{mn}(\mathbf{k}) = \varepsilon_m(\mathbf{k}) - \varepsilon_n(\mathbf{k})$ and $\tilde{\delta}_{mn} = 1 - \delta_{mn}$. $1/T_2 = 0.004$ a.u. is the relaxation parameter, and the corresponding dephasing time T_2 is approximately 6.1 fs. The transition dipole elements are $\mathbf{D}_{mn}(\mathbf{k}) = i \langle u_{m,\mathbf{k}}(\mathbf{r}) | \nabla_{\mathbf{k}} | u_{n,\mathbf{k}}(\mathbf{r}) \rangle$, where $u_{m,\mathbf{k}}(\mathbf{r})$ is the periodic part of the Bloch wavefunction for m band of graphene [28, 29].

In Eqs. (1), we have transformed the field-free crystal momentum \mathbf{K}_0 into a frame moving one $\mathbf{K}(t) = \mathbf{K}_0 + \mathbf{A}(t)$. $\mathbf{A}(t) = A_0 \sin^2(\omega_0 t/2n) \cos(\omega_0 t) \mathbf{e}$ is the vector potential of the infrared laser field with $n = 3$ and the amplitude of A_0 . ω_0 is the frequency of the IR laser field, corresponding to the wavelength of $\lambda = 5500$ nm. \mathbf{e} is the unit vector along the $\Gamma - M$ direction of graphene. The electric field of the laser is calculated by $\mathbf{E}(t) = -\partial \mathbf{A}(t)/\partial t$

The total current $\mathbf{j}_{\text{tot}}(t)$ is the sum of the intraband current $\mathbf{j}_{\text{tra}}(t)$ and the interband current $\mathbf{j}_{\text{ter}}(t)$, which can be evaluated by

$$\mathbf{j}_{\text{tra}}(t) = \sum_{m=c,v} \int_{\text{BZ}} \mathbf{p}_{mm}(\mathbf{K}(t)) \rho_{mm}(\mathbf{K}(t), t) d\mathbf{K}_0, \quad (2a)$$

$$\mathbf{j}_{\text{ter}}(t) = \int_{\text{BZ}} \mathbf{p}_{cv}(\mathbf{K}(t)) \rho_{vc}(\mathbf{K}(t), t) d\mathbf{K}_0 + \text{c.c.}, \quad (2b)$$

$$\mathbf{j}_{\text{tot}}(t) = \mathbf{j}_{\text{tra}}(t) + \mathbf{j}_{\text{ter}}(t), \quad (2c)$$

in which the transition dipole moments of the momentum operator consists of the intraband dipole elements $\mathbf{p}_{cc}(\mathbf{k}) = \nabla_{\mathbf{k}} \varepsilon_c(\mathbf{k}) = -\mathbf{p}_{vv}(\mathbf{k})$ and interband dipole elements $\mathbf{p}_{cv}(\mathbf{k}) = i(\varepsilon_c(\mathbf{k}) - \varepsilon_v(\mathbf{k})) \mathbf{D}_{cv}(\mathbf{k}) = -\mathbf{p}_{vc}(\mathbf{k})$. BZ denotes the first Brillouin zone.

The total yield of harmonic emission can be evaluated using

$$H_{\text{tot}}(\omega) = \omega^2 |F_{\text{tot}}(\omega)|^2, \quad (3)$$

in which $F_{\text{tot}}(\omega) = \int_{-\infty}^{\infty} \mathbf{e} \cdot \mathbf{j}_{\text{tot}}(t) e^{-i\omega t} dt$.

To reveal the generation mechanism of spectral caustics, we also calculate the time-frequency analysis of HHG using

$$H_{tf}(\omega, t) = \omega^2 |F_{tf}(\omega, t)|^2, \quad (4)$$

in which $F_{tf}(\omega, t) = \int_{t-T}^{t+T} dt' \mathbf{e} \cdot \mathbf{j}_{\text{tot}}(t') W(t' - t) e^{i\omega t'}$ where the window function $W(x) = \frac{1}{\sqrt{2\pi\tau_0}} e^{-x^2/2\tau_0^2}$ with $\tau_0 = 1/3\omega_0$. $T = 2\pi/\omega_0$ is the period of the laser field.

C. Time-dependent density functional theory

Since our density-matrix equations only consider two energy bands under the tight-binding approximation, we check our main results with time-dependent density functional theory (TDDFT) [30]. Within the TDDFT framework, the evolution of the wavefunction is computed by propagating the Kohn-Sham equations [31–33]: $i\frac{\partial}{\partial t}\psi_i(\mathbf{r}, t) = \hat{H}_{\text{KS}}(\mathbf{r}, t)\psi_i(\mathbf{r}, t)$, where $\psi_i(\mathbf{r}, t)$ is the wavefunction of an electron with the index i . \hat{H}_{KS} is the Kohn-Sham Hamiltonian in the velocity gauge given by $\hat{H}_{\text{KS}}(\mathbf{r}, t) = \frac{1}{2}[\hat{\mathbf{p}} + \mathbf{A}(t)]^2 + V_{\text{KS}}(\mathbf{r}, t)$, where $V_{\text{KS}}(\mathbf{r}, t) = V(\mathbf{r}, t) + V_{\text{Hartree}}[\mathbf{n}](\mathbf{r}, t) + V_{\text{xc}}[\mathbf{n}](\mathbf{r}, t)$ is the Kohn-Sham potential and $V_{\text{Hartree}}[\mathbf{n}](\mathbf{r}, t)$ is the Hartree potential. $\mathbf{n}(\mathbf{r}, t) = \sum_i |\psi_i(\mathbf{r}, t)|^2$ is the electron density. $V(\mathbf{r}, t)$ represents the interaction between four valence electrons and the ionic core, and is modeled by norm-conserving pseudopotentials. $V_{\text{xc}}[\mathbf{n}](\mathbf{r}, t)$ is the exchange-correlation potential. Here, we apply the generalized gradient approximation in the Perdew-Burke-Ernzerhof parametrization.

Before the graphene system is put into time-dependent evolution, the ground-state electronic structures are first generated from a density functional theory (DFT) calculation [34, 35]. The corresponding energy band results are shown in Fig. 1(c), where the black and red solid lines represent the v and c bands, respectively. In the calculation of the harmonic generation in graphene, a $60 \times 60 \times 1$ k-point mesh is used to sample the Brillouin zone, and the real-space spacing is $0.2 \text{ \AA} (\approx 0.378 \text{ a.u.})$. The vector potential $\mathbf{A}(t)$ of the laser field are the same as those used in the TBDMs. The OCTOPUS package [36, 37] is employed to perform the simulations.

III. CAUSTIC EFFECTS ON THE HIGH-ORDER HARMONIC GENERATION IN GRAPHENE

A. HOHG in the classical trajectory perspective

The interband current plays important role in the HOHG of graphene. It is useful to explore Eqs. (1) by using the Keldysh approximation [38] $\rho_{vv}(\mathbf{K}(t), t) \approx 1$ and $\rho_{cc}(\mathbf{K}(t), t) \approx 0$. Based on this approximation, the intraband current $\mathbf{j}_{\text{tra}}(t)$ is zero according to Eq. (2a). For the interband current $\mathbf{j}_{\text{ter}}(t)$, one can obtain $\pi_{cv}(\mathbf{K}(t), t) = -i \int_{-\infty}^t \mathbf{E}(t') \mathbf{D}_{cv}(\mathbf{K}(t')) e^{i \int_{-\infty}^{t'} \varepsilon_{cv}(\mathbf{K}(\tau)) d\tau} dt'$, in which $\pi_{cv}(\mathbf{K}(t), t) = \rho_{cv}(\mathbf{K}(t), t) e^{i \int_{-\infty}^t \varepsilon_{cv}(\mathbf{K}(\tau)) d\tau}$. Here, we have neglected the dephasing effect. The Fourier transform of the interband current is

$$\tilde{\mathbf{j}}_{\text{ter}}(\omega) = \int_{-\infty}^{\infty} dt \int d\mathbf{K}_0 \int_{-\infty}^t dt' g(\mathbf{K}_0, t', t) e^{iS(\mathbf{K}_0, t', t, \omega)} + \text{c.c.} \quad (5)$$

in which $S(\mathbf{K}_0, t', t, \omega) = \int_{t'}^t \varepsilon_{cv}(\mathbf{K}(\tau)) d\tau - \omega t$ is the semi-classical action. In contrast to the quickly oscillating exponent, $g(\mathbf{K}_0, t', t) = i \mathbf{p}_{cv}(\mathbf{K}(t)) \mathbf{E}(t') \mathbf{D}_{vc}(\mathbf{K}(t'))$ represents a slowly varying term. Hence, we can use the stationary phase approximation to solve Eq. (5). The saddle-point conditions are

$$\frac{\partial}{\partial t'} S(\mathbf{K}_0, t', t, \omega) = \varepsilon_{cv}(\mathbf{K}(t_i)), \quad (6a)$$

$$\begin{aligned} \nabla_{\mathbf{K}_0} S(\mathbf{K}_0, t', t, \omega) &= \int_{t_i}^{t_r} \nabla_{\mathbf{K}(\tau)} \varepsilon_{cv}(\mathbf{K}(\tau)) d\tau \\ &= \Delta x \mathbf{e}_x + \Delta y \mathbf{e}_y = 0, \end{aligned} \quad (6b)$$

$$\frac{\partial}{\partial t} S(\mathbf{K}_0, t', t, \omega) = \varepsilon_{cv}(\mathbf{K}(t_r)) - \omega = 0, \quad (6c)$$

in which t_i and t_r correspond to t' and t that satisfy the saddle-point conditions, and represent the birth and recombination times of electron-hole pair, respectively. \mathbf{e}_x and \mathbf{e}_y are unit vectors along x and y directions, respectively. Δx and Δy are relative displacements of electron-hole pair in two directions.

Equation (5) can be deduced to be

$$\tilde{\mathbf{j}}_{\text{ter}}(\omega) \propto \sum_{\mathbf{K}_{st}, t_i, t_r} g(\mathbf{K}_{st}, t_i, t_r) \frac{e^{iS(\mathbf{K}_{st}, t_i, t_r, \omega)}}{|\det(S''(\mathbf{K}_{st}, t_i, t_r, \omega))|}, \quad (7)$$

in which \mathbf{K}_{st} is the crystal momentum \mathbf{K}_0 that agrees with the recombination condition of Eqs. (6). $S''(\mathbf{K}_{st}, t_i, t_r, \omega)$ is the Hessian matrix of the classical action $S(\mathbf{K}_{st}, t_i, t_r, \omega)$. The determinant of $S''(\mathbf{K}_{st}, t_i, t_r, \omega)$ is

$$\begin{aligned} \det(S'') &= \begin{vmatrix} b & -\mathbf{a}(t_i) & \mathbf{a}(t_r) \\ \mathbf{a}(t_i) & -\mathbf{E}(t_i) \mathbf{a}(t_i) & 0 \\ \mathbf{a}(t_r) & 0 & -\mathbf{E}(t_r) \mathbf{a}(t_r) \end{vmatrix} \\ &= \mathbf{a}(t_i) \cdot \mathbf{a}(t_r) \{ \mathbf{a}(t_i) \cdot \mathbf{E}(t_r) + \mathbf{E}(t_i) \cdot [\mathbf{a}(t_r) + b \mathbf{E}(t_r)] \}, \end{aligned} \quad (8)$$

in which $\mathbf{a}(t) = \nabla_{\mathbf{K}(t)} \varepsilon_{cv}(\mathbf{K}(t))$, $b = \int_{t_i}^{t_r} \nabla_{\mathbf{K}(\tau)}^2 \varepsilon_{cv}(\mathbf{K}(\tau)) d\tau$ and we set $c(\mathbf{K}_{st}, t_i, t_r) = \mathbf{a}(t_i) \cdot \mathbf{E}(t_r) + \mathbf{E}(t_i) \cdot [\mathbf{a}(t_r) + b \mathbf{E}(t_r)]$ in the following.

According to Eqs. (7) and (8), the harmonic caustic effect appears at $\det(S'') = \mathbf{a}(t_r) \cdot \mathbf{a}(t_i) c(\mathbf{K}_{st}, t_i, t_r) = 0$. Here, one can find that $|\mathbf{a}(t_i)|$ and $|\mathbf{a}(t_r)|$ are closely related to the density of states at the ionization and recombination times. For the caustic condition of $|\mathbf{a}(t_r)| = 0$, which imply that the density of states $N(\omega) \propto 1/|\mathbf{a}(t_r)|$ exhibits singularities, the corresponding caustic effects have been observed in Ref. [19]. In addition, in Ref. [18], authors have proposed that for the one-dimensional period solid, the caustic effects appear when the different branches of electron-hole trajectories coalesce into a single branch, corresponding to the condition of $c(\mathbf{K}_{st}, t_i, t_r) = 0$. In the following, we investigate the caustic effects of the two-dimensional graphene system.

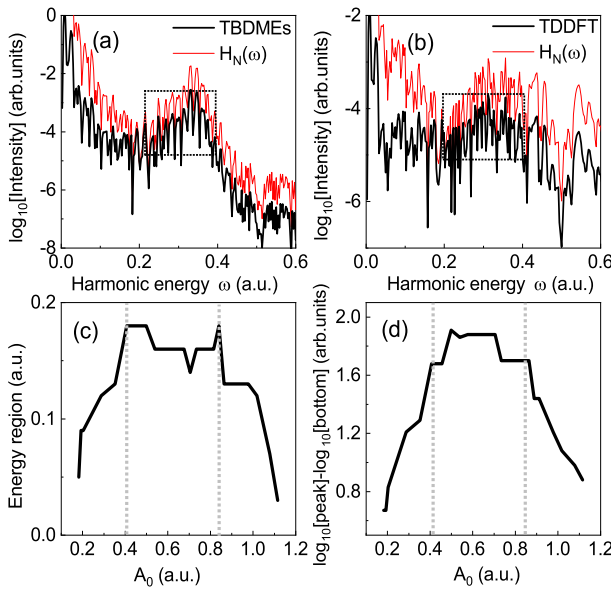


Figure 2. HOHG spectra calculated by TBDME (a) and TDDFT (b) with the laser intensity of $8 \times 10^{11} \text{ W/cm}^2$ and the wavelength of 5500 nm. In panels (a) and (b), the dotted rectangles indicate the caustic structures. The energy region (c) and the peak-bottom intensity difference (d) of the caustic structures, which are the width and height of the dotted rectangles in (a), respectively, as a function of the amplitude of laser vector potential.

B. Caustic structures in HOHG of graphene

In Figs. 2(a) and 2(b), the black curves are the harmonic spectra of graphene calculated by the TBDMEs and TDDFT, respectively, where the intensity of the laser is $8 \times 10^{11} \text{ W/cm}^2$ and the wavelength is 5500 nm. One can find that for both simulations, the harmonic spectra are qualitatively consistent and present clear enhancements in the region of the dotted rectangles, which may arise from caustic effects on the HOHG in graphene.

Based on TBDMEs, we also calculate the caustic structures of other laser intensities. In Figs. 2(c) and 2(d), we show the energy range and the peak-bottom intensity difference of the caustic structures, which are the width and height of the dotted rectangles in Figs. 2(a) and 2(b), respectively, as a function of the amplitude of laser vector potential. From Figs. 2(c) and 2(d), one can find that the caustic effects enhance for laser vector potential from 0.2 to 0.4 a.u., then remain stable at the region from 0.4 to 0.84 a.u., and finally weaken as the vector potential increases further.

For graphene, the electrons easily ionized from the valence band to the conduction band are located around the Dirac points. Therefore, it may be difficult to obtain $|\mathbf{a}(t_i)| = 0$. Considering that $|\mathbf{a}(t_r)|$ are closely related to the density of states $N(\omega)$ of graphene, in Figs. 2(a) and 2(b), the red curves present the harmonic in-

tensity $H_N(\omega) = \omega^2 |F(\omega)/N(\omega)|^2$. One can obtain that the caustic structures are further enhanced, which implies that the caustic effects of graphene may arise from $c(\mathbf{K}_{st}, t_i, t_r) = 0$.

C. Caustic trajectory

Figure 3(a) shows the time-frequency analysis $\log_{10}(H_{tf}(\omega, t))$ of the harmonic spectrum that is calculated by TBDME with the laser intensity of $8 \times 10^{11} \text{ W/cm}^2$. One can find that for the region indicated by the dotted rectangles, the harmonic yield is clearly enhanced, corresponding to the caustic structures shown in Fig. 2(a).

In Figs. 3(b), 3(c) and 3(d), the green dots are the lattice momenta \mathbf{K}_{st} , $\mathbf{K}(t_i)$ and $\mathbf{K}(t_r)$, respectively, which are calculated by Eqs. (6). As mentioned above, electrons of the first Brillouin zone are transformed by $\mathbf{K}(t) = \mathbf{K}_{st} + \mathbf{A}(t)$. According to Eq. (6a), we assume that the electron-hole pair can generate at time t_i with any energy gaps, and we ignore the imaginary part of the ionization time. Next, the electron and hole move in the real two-dimensional space with the relative velocity of $\nabla_{\mathbf{K}(t)} \varepsilon_{cv}(\mathbf{K}(t))$. As shown by Eq. (6b), when the relative position of the electron-hole pair is 0 again, they reencounter each other and the recombination time t_r can be obtained. Utilizing $\mathbf{K}(t_r) = \mathbf{K}(t_i) - \mathbf{A}(t_i) + \mathbf{A}(t_r)$ and Eq. (6c), one can obtain the emitted harmonic energy $\omega = \varepsilon_{cv}(\mathbf{K}(t_r))$.

Note that in contrast to other solids [19, 28], the energy gaps are zero at the Dirac points for graphene. Not only exactly at the Dirac points, but electrons around the Dirac points can also be ionized, therefore, we further relax the ionization condition to all energy gaps. In addition, we strictly require perfect electron-hole collision instead of imperfect recollisions [39–41]. Finally, in the calculations, we only have considered the first recombination of electron-hole pair.

Next, from the green dots in Figs. 3(b), 3(c) and 3(d), we further extract the black lines that satisfy the caustic condition of $c(\mathbf{K}_{st}, t_i, t_r) = 0$. The corresponding harmonic energy $\varepsilon_{cv}(\mathbf{K}(t_r))$ as a function of emitted time t_r also have been shown by the black line in Fig. 3(a), and one can find that the time-frequency results of Fig. 3(a) are consistent with the caustic results.

To reveal the mechanism of the caustic effect more clearly, we extract a one-dimensional section of $\mathbf{k}_y = -0.59 \text{ a.u.}$ in the graphene reciprocal space. Figure 4(a) presents $\omega = \varepsilon_{cv}(\mathbf{K}(t_r))$ and $c(\mathbf{K}_{st}, t_i, t_r)$ as a function of initial lattice momenta $\mathbf{K}_{st} = (\mathbf{K}_{st,x}, -0.59 \text{ a.u.})$. One can find that corresponding to the singularity of $1/|det(S'')|$ with $c(\mathbf{K}_{st}, t_i, t_r) = 0$, the recombination energy approaches to the maximum, where two branches of trajectories coalesce into a single trajectory.

In Fig. 4(b), we show the time-dependent transformations of the electron lattice momenta. The initial (\mathbf{K}_{st}), birth ($\mathbf{K}(t_i)$) and recombination lattice momenta

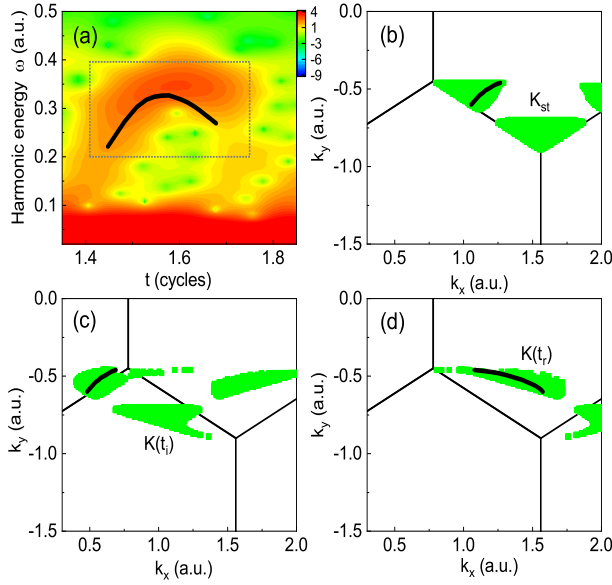


Figure 3. (a) The time-frequency analysis of the harmonic spectrum simulated by TBDME for the intensity of $8 \times 10^{11} \text{ W/cm}^2$, which is calculated by $\log_{10}(H_{tf}(\omega, t))$ of Eq. (4). In panels (b), (c) and (d), the green points are the lattice momenta \mathbf{K}_{st} , $\mathbf{K}(t_i)$ and $\mathbf{K}(t_r)$. The black points are the lattice momenta that satisfy caustic condition of $c(\mathbf{K}_{st}, t_i, t_r) = 0$.

$(\mathbf{K}(t_r))$ of electron-hole pairs are marked by the black points. The dotted lines indicate the harmonic energies $\varepsilon_{cv}(\mathbf{K}(t_r))$ corresponding to $\mathbf{K}(t_r)$. The red line in Fig. 4(b) is the trajectory that satisfies caustic condition of $c(\mathbf{K}_{st}, t_i, t_r) = 0$. One can find that around the red line, the recombination energies of other trajectories are close to that of the red trajectory.

In Figs. 4(c) and 4(d), we present the results of $k_y = -0.55 \text{ a.u.}$. Similar to that of $k_y = -0.59 \text{ a.u.}$, Fig. 4(c) also shows that two branches of harmonic trajectories coalesce into a single trajectory at $c(\mathbf{K}_{st}, t_i, t_r) = 0$, which corresponds to the red line in Fig. 4(d). For other k_y , the similar results can be presented. All caustic trajectories of $c(\mathbf{K}_{st}, t_i, t_r) = 0$ make up the black line $\omega = \varepsilon_{cv}(\mathbf{K}(t_r))$ in Fig. 3(a), which agrees with the time-frequency analysis. In contrast to atom, for which the caustic is a point where the long and short trajectories of recollision electrons coalesce into a single trajectory (See Appendix A for detail), the caustic effects of two-dimensional graphene are a line.

IV. CONCLUSION AND DISCUSSION

In summary, we have investigated the caustic effects on the HOHG in graphene. We numerically simulate the HOHG by the two-band density-matrix equations and time-dependent density functional theory, respectively, and the both results present obvious caustic structures.

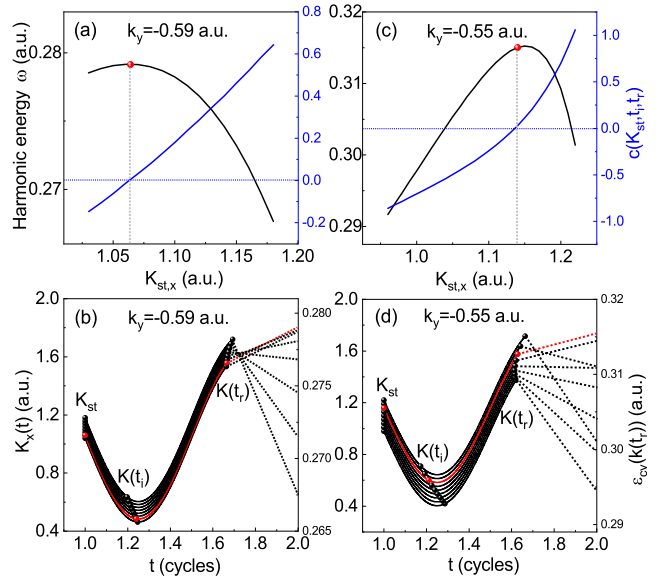


Figure 4. (a) The harmonic energy and $c(\mathbf{K}_{st}, t_i, t_r)$ with $\mathbf{K}_{st} = (\mathbf{K}_{st,x}, -0.59 \text{ a.u.})$ as a function of the lattice momenta $\mathbf{K}_{st,x}$ for the one-dimensional section $k_y = -0.59 \text{ a.u.}$ of the graphene reciprocal space. (b) Corresponding to (a), in the reciprocal space, the transformation of typical electrons as a function of the laser period. Here, t_i and t_r are the birth and recombination times of electron-hole pair, and the dotted lines indicate the recombination energy $\varepsilon_{cv}(\mathbf{K}(t_r))$ corresponding to $\mathbf{K}(t_r)$. (c),(d) Same as (a) and (b), respectively, but $k_y = -0.55 \text{ a.u.}$

Further calculations show that the caustic effects exist over a wide range of laser vector potential from 0.4 to 0.84 a.u.. Based on the classical trajectory of electrons in the real space, we reveal the underlying mechanism of the caustic effects. For a one-dimensional section of the graphene reciprocal space, when the different branches of electron-hole trajectories generating high-order harmonics coalesce into a single branch, caustic effects appear. In contrast to atom and one-dimensional solid, in which the caustic effects usually appear at a or a few specific harmonic energies, for the two-dimensional graphene system, the caustic effects emerge in broad, continuous energy regions, which dominates interband harmonic generation.

ACKNOWLEDGMENTS

This work is supported by NSAF (Grant No. U1930403). We acknowledge valuable discussions with Professor Qinzhixia.

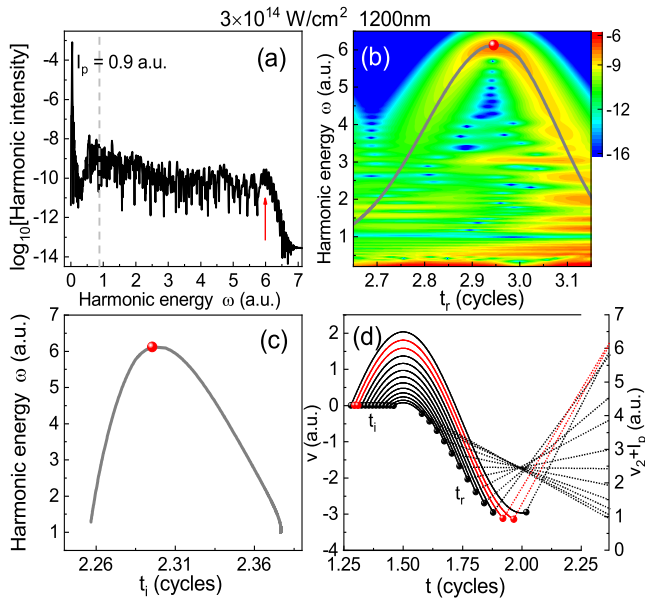


Figure 5. (a) The harmonic spectrum of the model atom, which is calculated by one-dimensional TDSE simulations. (b) The time-frequency analysis of the harmonic spectrum. In panels (b) and (c), the grey lines present the harmonic energy as a function of the emission time and ionized time, respectively. (d) Trajectories of electrons that are ionized at different times in velocity space.

Appendix A: Caustic effects on the high-order harmonic generation in model atom

We also investigate the caustic effects on HOHG of a model atom. The Hamiltonian of the model atom here

is $H(t) = p^2/2 + V(x) + xE(t)$ with the soft-Coulomb potential $V(x) = -Z/\sqrt{\varepsilon + x^2}$. Here, we set the effective charge $Z = 1$ a.u. as well as the smoothing parameter $\varepsilon = 0.5$ to ensure that the ionization potential of the model atom is $I_p = 0.9$ a.u., which is consistent with the ionization energy of helium atoms. The electric field used here is $E(t) = f(t)E_0 \sin(\omega_0 t)$. $f(t)$ is the sine square envelope function. E_0 and ω_0 are the amplitude and the frequency of laser field, and the corresponding laser intensity and the wavelength are 3×10^{14} W/cm² and 1200 nm. The numerical results are calculated by solving the one-dimensional time-dependent Schrödinger equation (TDSE) $i\dot{\Psi}(t) = H(t)\Psi(t)$ by the spectral method [42]. With the TDSE wave function $\Psi(t)$, the coherent part of the spectrum can be evaluated using $F_{\text{atom}}(\omega) = \int \langle \Psi(t) | \nabla V(x) | \Psi(t) \rangle e^{-i\omega t} dt$ and the harmonic intensity is $H_{\text{atom}}(\omega) = |F_{\text{atom}}(\omega)|^2$.

In Fig. 5(a) and 5(b), we show the harmonic spectrum and its time-frequency analysis. One can find the high yield of harmonic spectrum around harmonic energy of 6 a.u., as indicated by the red arrow in Fig. 5(a) and the black point in Fig. 5(b).

In Figs. 5(b) and 5(c), the grey lines present the harmonic energy as a function of the harmonic emission time and ionized time of electrons, respectively. Figure 5(d) shows the trajectories of electrons in velocity space. They are all calculated by the simple-man model. The black points in Figs. 5(b) and 5(c) are the singularity, where the long and short trajectories of recollision electrons coalesce into a single trajectory, has been known to cause caustic enhancement in the spectrum. The red trajectories in Fig. 5(d) corresponding to the black points of Figs. 5(b) and 5(c) are the caustic trajectories, which clearly show that different trajectories contribute to the same energy.

[1] O. Raz, O. Pedatzur, B. D. Bruner, and N. Dudovich, Spectral caustics in attosecond science, *Nat. Photonics* **6**, 170 (2012).

[2] M. Berry, and C. Upstill, *Catastrophe Optics: Morphologies of Caustics and their Diffraction Patterns*, (Elsevier, 1980).

[3] Y. A. Kravtsov, and Y. I. Orlov, Caustics, catastrophes, and wave fields, *Sov. Phys. Usp.* **26**, 1038 (1983).

[4] P. B. Corkum, Plasma perspective on strong field multi-photon ionization, *Phys. Rev. Lett.* **71**, 1994 (1993).

[5] M. Lewenstein, Ph. Balcou, M. Yu. Ivanov, A. L'Huillier, and P. B. Corkum, Theory of high-harmonic generation by low-frequency laser fields, *Phys. Rev. A* **49**, 2117 (1994).

[6] J. Itatani, J. Levesque, D. Zeidler, H. Niikura, H. Pépin, J. C. Kieffer, P. B. Corkum, and D. M. Villeneuve, Tomographic imaging of molecular orbitals, *Nature* **432**, 867 (2004).

[7] M. Meckel, D. Comtois, D. Zeidler, A. Staudte, D. Pavičić, H. C. Bandulet, H. Pépin, J. C. Kieffer, R. Dörner, D. M. Villeneuve, and P. B. Corkum, Laser-induced electron tunneling and diffraction, *Science* **320**, 1478 (2008).

[8] T. T. Luu, M. Garg, S. Yu. Kruchinin, A. Moulet, M. Th. Hassan, and E. Goulielmakis, Extreme ultraviolet high-harmonic spectroscopy of solids, *Nature* **521**, 498 (2015).

[9] G. Vampa, T. J. Hammond, N. Thiré, B. E. Schmidt, F. Légaré, C. R. McDonald, T. Brabec, and P. B. Corkum, Linking high harmonics from gases and solids, *Nature* **522**, 462 (2015).

[10] M. Hohenleutner, F. Langer, O. Schubert, M. Knorr, U. Huttner, S. W. Koch, M. Kira, and R. Huber, Real-time observation of interfering crystal electrons in high-harmonic generation, *Nature* **523**, 572 (2015).

[11] S. Ghimire, A. D. DiChiara, E. Sistrunk, P. Agostini, L. F. DiMauro, and D. A. Reis, Observation of high-order harmonic generation in a bulk crystal, *Nat. Phys.* **7**, 138 (2011).

[12] G. Ndabashimiye, S. Ghimire, M. X. Wu, D. A. Browne, K. J. Schafer, M. B. Gaarde, and D. A. Reis, Solid-state harmonics beyond the atomic limit, *Nature* **534**,

520 (2016).

[13] H. Z. Liu, Y. L. Li, Y. S. You, S. Ghimire, T. F. Heinz, and D. A. Reis, High-harmonic generation from an atomically thin semiconductor, *Nat. Phys.* **13**, 262 (2017).

[14] K. Kaneshima, Y. Shinohara, K. Takeuchi, N. Ishii, K. Imasaka, T. Kaji, S. Ashihara, K. L. Ishikawa, and J. Itatani, Polarization-resolved study of high harmonics from bulk semiconductors, *Phys. Rev. Lett.* **120**, 243903 (2018).

[15] D. Faccialà, S. Pabst, B. D. Bruner, A. G. Ciriolo, S. De Silvestri, M. Devetta, M. Negro, H. Soifer, S. Stagira, N. Dudovich, and C. Vozzi, Probe of Multielectron Dynamics in Xenon by Caustics in High-Order Harmonic Generation, *Phys. Rev. Lett.* **117**, 093902 (2016).

[16] K. R. Hamilton, H. W. van der Hart, and A. C. Brown, Pulse-shape control of two-color interference in high-order-harmonic generation, *Phys. Rev. A* **95**, 013408 (2017).

[17] E. Pisanty, M. F. Ciappina, and M. Lewenstein, The imaginary part of the high-harmonic cutoff, *J. Phys. Photon.* **2**, 034013 (2020).

[18] J. Chen, Q. Xia, and L. Fu, Spectral caustics of high-order harmonics in one-dimensional periodic crystals, *Opt. Lett.* **46**, 2248 (2021).

[19] A. J. Uzan, G. Orenstein, Á. Jiménez-Galán, C. McDonald, R. E. F. Silva, B. D. Bruner, N. D. Klimkin, V. Blanchet, T. Arusi-Parpar, M. Krüger, A. N. Rubtsov, O. Smirnova, M. Ivanov, B. Yan, T. Brabec, and N. Dudovich, Attosecond spectral singularities in solid-state high-harmonic generation, *Nat. Photonics* **14**, 183 (2020).

[20] P. R. Wallace, The band theory of graphite, *Phys. Rev.* **71**, 622 (1947).

[21] A. H. Castro Neto, F. Guinea, N. M. R. Peres, K. S. Novoselov, and A. K. Geim, The electronic properties of graphene, *Rev. Mod. Phys.* **81**, 109 (2009).

[22] N. Yoshikawa, T. Tamaya, and K. Tanaka, High-harmonic generation in graphene enhanced by elliptically polarized light excitation, *Science* **356**, 736 (2017).

[23] I. A. Calafell, L. A. Rozema, D. A. Iranzo, A. Trenti, P. K. Jenke, J. D. Cox, A. Kumar, H. Bieliaiev, S. Nanot, C. Peng, D. K. Efetov, J. Y. Hong, J. Kong, D. R. Englund, F. J. García de Abajo, F. H. L. Koppens, and P. Walther, Giant enhancement of third-harmonic generation in graphene metal heterostructures, *Nat. Nanotechnol.* **16**, 318 (2021).

[24] F. Dong, Q. Xia, and J. Liu, Ellipticity of the harmonic emission from graphene irradiated by a linearly polarized laser, *Phys. Rev. A* **104**, 033119 (2021).

[25] H. K. Kelardeh, U. Saalmann, and J. M. Rost, Ultra-short laser-driven dynamics of massless Dirac electrons generating valley polarization in graphene, *Phys. Rev. Research* **4**, L022014 (2022).

[26] F. Dong, and J. Liu, Knee structure in the laser-intensity dependence of harmonic generation for graphene, *Phys. Rev. A* **106**, 043103 (2022).

[27] W. V. Houston, Acceleration of electrons in a crystal lattice, *Phys. Rev.* **57**, 184 (1940).

[28] G. Vampa, C. R. McDonald, G. Orlando, D. D. Klug, P. B. Corkum, and T. Brabec, Theoretical Analysis of High-Harmonic Generation in Solids, *Phys. Rev. Lett.* **113**, 073901 (2014).

[29] S. C. Jiang, H. Wei, J. G. Chen, C. Yu, R. F. Lu, and C. D. Lin, Effect of transition dipole phase on high-order harmonic generation in solid materials, *Phys. Rev. A* **96**, 053850 (2017).

[30] C. A. Ullrich, *Time-Dependent Density-Functional Theory: Concepts and Applications* (Oxford University Press, Oxford, 2011).

[31] M. Marques, E. Gross, Time-dependent density functional theory, *Annu. Rev. Phys. Chem.* **55**, 427 (2004).

[32] Z. Nourbakhsh, N. Tancogne-Dejean, H. Merdji, and A. Rubio, High harmonics and isolated attosecond pulses from MgO, *Phys. Rev. Appl.* **15**, 014013 (2021).

[33] G. L. Breton, A. Rubio, and N. Tancogne-Dejean, High-harmonic generation from few-layer hexagonal boron nitride: Evolution from monolayer to bulk response, *Phys. Rev. B* **98**, 165308 (2018).

[34] P. Hohenberg, and W. Kohn, Inhomogeneous electron gas, *Physical Review* **136** B864 (1964).

[35] W. Kohn, L. J. Sham, Self-consistent equations including exchange and correlation effects, *Physical Review* **140** A1133 (1965).

[36] X. Andrade, D. A. Strubbe, U. D. Giovannini, A. H. Larsen, M. J. T. Oliveira, J. Alberdi-Rodriguez, A. Varas, I. Theophilou, N. Helbig, M. Verstraete, L. Stella, F. Nogueira, A. Aspuru-Guzik, A. Castro, M. A. L. Marques, and A. Rubio, Real-space grids and the octopus code as tools for the development of new simulation approaches for electronic systems, *Phys. Chem. Chem. Phys.* **17**, 31371 (2015).

[37] A. Castro, M. A. L. Marques, and A. Rubio, Propagators for the time-dependent kohn-sham equations, *J. Chem. Phys.* **121**, 3425 (2004).

[38] L. Keldysh, Ionization in the field of a strong electromagnetic wave, *Sov. Phys. JETP* **20**, 1307 (1965).

[39] L. Yue and M. B. Gaarde, Imperfect Recollisions in High-Harmonic Generation in Solids, *Phys. Rev. Lett.* **124**, 153204 (2020).

[40] A. M. Parks, G. Ernott, A. Thorpe, C. R. McDonald, P. B. Corkum, M. Taucer, and T. Brabec, Wannier quasi-classical approach to high harmonic generation in semiconductors, *Optica* **7**, 1764 (2020).

[41] Y. Feng, S. Shi, J. Li, Y. Ren, X. Zhang, J. Chen, and H. Du, Semiclassical analysis of ellipticity dependence of harmonic yield in graphene, *Phys. Rev. A* **104**, 043525 (2021).

[42] M. D. Feit, J. A. FleckJr., and A. Steiger, Solution of the Schrödinger equation by a spectral method, *J. Comput. Phys.* **47**, 412 (1982).

[*] jliu@gscaep.ac.cn